Carbohydrate Polymers 264 (2021) 118026

Contents lists available at ScienceDirect

Carbohydrate Polymers

journal homepage: www.elsevier.com/locate/carbpol

3D printed alginate-cellulose nanofibers based patches for local curcumin administration

R. Olmos-Juste [a], B. Alonso-Lerma [b], R. Pérez-Jiménez [b], N. Gabilondo [a,*], A. Eceiza [a,*]

[a] 'Materials + Technologies' Research Group (GMT), Department of Chemical and Environmental Engineering, Faculty of Engineering of Gipuzkoa, University of the Basque Country, Plaza Europa 1, Donostia-San Sebastian, 20018, Spain
[b] CIC nanoGUNE BRTA, San Sebastian, Spain

ARTICLE INFO

Keywords:
Alginate
Nanocellulose
Bioink
3D printing
Curcumin
Drug release

ABSTRACT

Alginate and nanocellulose are potential biomaterials to be employed as bioinks for three-dimensional (3D) printing. Alginate-cellulose nanofibers (A-CNF) formulations with CNF amounts up to 5 wt% were developed and rheologically characterized to evaluate their printability. Results showed that formulations with less than 3 wt% CNF did not present suitable characteristics to ensure shape fidelity after printing. Selected A-CNF bioinks were 3D printed and freeze-dried to obtain porous scaffolds. Morphological and mechanical analysis were performed, showing that CNF contributed to the reinforcement of the scaffolds and modulated their porosity. The applicability for drug delivery was evaluated by the addition of curcumin to printable A-CNF formulations. The curcumin loaded bioinks were successfully 3D printed in patches and the *in vitro* release tests showed that alginate and CNF played an important role in curcumin stabilization, whereas the CNF content and the disintegration of the scaffold were essential in the release kinetics.

1. Introduction

Additive manufacturing technology, most commonly known as 3D printing, is nowadays intensively being invested as it presents multiple interests for biomedical applications (Gao et al., 2016). Among them, these techniques represent an opportunity to develop safer and more efficient drug dosage customized delivery systems. Syringe extrusion printing is the most common 3D printing technique used for pharmaceutical purposes (Jose et al., 2016; Placone & Engler, 2018). Materials for pharmaceutical uses in syringe extrusion 3D printing such as alginate, chitosan, gelatin or collagen are known as bioinks (Jose et al., 2016; Tappa & Jammalamadaka, 2018), whose application for human uses as food additive, drug excipient or wound dressing has to be approved by the Food and Drug Administration (FDA).

The suitability of any developed formulation to be used as bioink for 3D printing has to be thoroughly assessed, since they should present specific viscoelastic properties guaranteeing printability and shape fidelity, avoiding collapse of the printed samples (Gao et al., 2018; Hölzl et al., 2016; Schwab et al., 2020). Thus, the complete rheological characterization of the bioink results are crucial in order to predict how the material will perform during 3D printing, and the final printed shape. Firstly, bioinks must show shear-thinning behavior, which involves solid-like structure at zero shear rates and yet enough fluid behavior from a value of shear stress or high shear rates, when the material is extruded through the nozzle. In addition, the material must be able to recover the initial gel-like structure after the printing process when the shear stress is removed (Abouzeid et al., 2018; Hölzl et al., 2016).

In the last years, high molecular weight natural polymers such as alginate, collagen, hyaluronic acid or chitosan, have been widely investigated in 3D printing as bioinks because of their printability, biocompatibility and biodegradability, and they are approved by FDA (Jia et al., 2014; Kyle et al., 2017). Sodium alginate (SA) is a linear polysaccharide extracted from brown algae that is composed of 1-4-linked β-D-mannuronate (M) and α-L-guluronate (G) units arranged in MM and GG repeating or MG alternating blocks, varying depending on the source (Khouri & Buss, 2011). SA solutions are non-Newtonian fluids with suitable rheological properties to be extruded through a nozzle (Li et al., 2016). Nevertheless, SA solutions do not have appropriate viscoelastic characteristics and solid-like behavior to overcome shape fidelity and mechanical strength problems after 3D printing (Heggset et al., 2019; Markstedt et al., 2015). Ma et al. (2014) reported that increasing of the SA content in the solution contributed to rise viscosity requirements, but not enough elastic behavior. Therefore, SA

* Corresponding authors.
E-mail addresses: nagore.gabilondo@ehu.eus (N. Gabilondo), arantxa.eceiza@ehu.eus (A. Eceiza).

https://doi.org/10.1016/j.carbpol.2021.118026
Received 17 November 2020; Received in revised form 24 March 2021; Accepted 27 March 2021
Available online 2 April 2021

based formulations require rheological modifiers to achieve optimal viscoelastic characteristics for syringe extrusion 3D printing and overcome the limitations related to shape fidelity and collapse (Heggset et al., 2019). One of the rheological modifiers that most interest is arousing in recent times is nanocellulose, both as cellulose nanofibers (CNF) and cellulose nanocrystals (CNC), due to its low density, sustainability and biocompatibility (Leppiniemi et al., 2017; Siqueira et al., 2017). Moreover, the high content of hydroxyls groups at their surface results in numerous effective interactions with many natural polymers, is efficiently integrated into the polymeric matrix (Abouzeid et al., 2018). In addition, the high length/diameter (L/D) aspect ratio and elevated specific mechanical properties of nanocellulose lead to increasing strength and resistance of the resulting material (Pei et al., 2011). Several investigations have been reported focusing on SA-CNF formulations with the aim of fabricate porous structures for tissue engineering use 3D printing technology (Abouzeid et al., 2018; Markstedt et al., 2015; Müller et al., 2017). Freeze-drying technique is widely used after 3D printing of water based bioinks, which allows maintaining the designed shape and the formation of nanoporous structures, also known as aerogels (Abdelwahed et al., 2006; Naseri et al., 2016). These 3D printed porous scaffolds show great swelling capacity, which can facilitate the release of many drugs and molecules of interest, being suitable to be used as drug delivery systems (Jia et al., 2014).

Customized localized drug delivery systems with patient drug requirements and particular drug dosages could be fabricated by 3D printing technology (Lee et al., 2019; Sultan et al., 2019). The development of drug delivery new devices is currently focused on cancer treatment due to the enormous impact of this disease in society (Hossen et al., 2019). The different drug delivery systems used for tumor treatment can be classified depending on the route of administration as systemic or localized (Ordikhani et al., 2016). Systemic drug delivery systems are focused on targeting applications while localized systems are used for *in situ* drug administration, avoiding systemic circulation and drug waste (Ordikhani et al., 2016).

Along with the delivery systems, numerous investigations are focused on the use of natural drugs for cancer therapies. However, in some cases, these natural bioactives present solubility limitations in physiological conditions, which directly implies bioavailability and pharmacodynamics issues to overcome. Curcumin, extracted from *Curcuma longa,* is a good example of a natural drug, broadly known because of its application in food industry and more recently in pharmaceutical field (Maheshwari et al., 2006; Mohanty & Sahoo, 2010). Biomedical uses of curcumin has been studied, proposing this molecule as a strong candidate for treating diseases such as Alzheimer, cystic fibrosis and multiple inflammatory diseases, as well as cancer prevention and treatment (Maheshwari et al., 2006; Yallapu et al., 2012), due to its ability to suppress the expression of some associated grown factors (Kunnumakkara et al., 2008). Curcumin is also known for its antimicrobial activity, which implies an advantage for biomedical purposes (Anagha et al., 2019). This drug is usually administrated in oral dosages, but its poor bioavailability is delimiting the treatment efficiency (Mohanty & Sahoo, 2010). *In situ* curcumin stabilization and release would improve its bioavailability and pharmacodynamics in targeted tumor. Dey and Sreenivasan (2014) proved that curcumin could be stabilized by an alginate solution. Moreover, cellulose nanoentities can also help to curcumin stabilization and release (Buffiere et al., 2017; Gómez et al., 2016; Li et al., 2013).

Therefore, the aim of this work was the design of a 3D printed patch loaded with curcumin to be used as drug delivery system in local disease treatment. For that purpose, firstly, alginate-cellulose nanofibers (A-CNF) formulations were developed as suitable bioinks for 3D printing technology and complete rheological characterization was performed in order to assess their printability and shape fidelity. Finally, curcumin was loaded in the selected A-CNF formulations and drug release from 3D printed patches was *in vitro* assessed. In this way, developed bioinks from biomaterials such as alginate and CNF for 3D printing technology are suitable not only to create specific designed scaffolds with high accuracy by this technique, but also could be employed as a carrier for hydrophobic drugs like curcumin; as well as for the design many other customized scaffolds for potential biomedical applications.

2. Experimental

2.1. Materials

Medium viscosity alginic acid sodium salt from brown algae (A2033); $M_W = 2.4 \times 10^5$ g mol^{-1} (calculated at 25 °C in NaCl 0.1 M from viscosity measurements) and M/G ratio of 1.56, was purchased from Sigma-Aldrich. Cellulose nanofibers (CNF, Lot. 9004-34-6) were bought from Maine University (USA). Commercial PBS (Phosphate Buffer Saline, pH = 7.4) tablets were purchased from PanReac. Dulbecco's Modified Eagle Medium (DMEM) was obtained from Gibco, Paisley (UK). DAPI (4′,6-diamidino-2-phenylindole) was purchased from Thermofisher. Curcumin from *Curcuma longa* (Turmeric, >65 %) was acquired from Sigma-Aldrich.

2.2. Methods and characterization

2.2.1. Preparation of A-CNF based bioinks

Five bioink formulations were prepared from alginate and CNF. Dispersions with different CNF content were prepared by mixing the required amount of CNF at concentrations of 1, 2, 3, 4 and 5 wt% in 60 mL of distilled water, blended using an Ultraturrax for 15 min at 12000 rpm and then ultrasonicated for 2 h. Alginate powder was added to the CNF dispersions at 4 wt% and mixed with an Ultraturrax until complete homogenization. Samples were maintained refrigerated along the whole procedure keeping them in an ice-bath to avoid heating and water evaporation during the sonication and mixing processes. The prepared formulations were denoted as A-CNFX, being X the CNF content (wt %) in the bioink. Drug delivery system formulations were prepared in the most suitable bioink formulations based on the rheological analyses, by adding 15 wt% of curcumin concentration in respect to the total A-CNF amount, following similar procedures found in the literature (Yakub et al., 2016). Formulations containing curcumin were designed as A-CNFX-cur.

2.2.2. 3D Printing of A-CNF based bioinks

A-CNF and A-CNF-cur bioinks were printed with a Voladora 3D printer (Tumaker, S.L. Spain) adapted for layer-by-layer syringe extrusion 3D printing. 3D structures with different shapes and sizes were printed (dog bone tensile test samples, cylinders of 15 mm in diameter and 10 or 5 mm in height and prisms of $25 \times 25 \times 4$ mm^3 (length × width × height)). All structures were printed at room temperature with a needle of 0.8 mm in diameter and speed of 4 mm s^{-1}. Resulted printed structures were freeze-dried at -80 °C and 0.1 mbar for 48 h to obtain porous scaffolds.

2.2.3. Fourier transform infrared spectroscopy (FTIR)

The characteristic functional groups of the CNF, alginate matrix, curcumin and A-CNF and A-CNF-cur freeze-dried scaffolds were analyzed by FTIR using a Nicolet Nexus spectrophotometer with a Specac MKII Golden Gate accessory with a diamond crystal at a nominal incidence angle of 45° and ZnSe lens. Spectra were recorded between 4000 and 650 cm^{-1} and 32 scans, with a resolution of 4 cm^{-1}.

2.2.4. X-Ray powder diffraction (XRD)

CNF crystallinity was determined by XRD using a Philips X'pert PRO automatic diffractometer performing at 40 kV and 40 mA, in theta-theta configuration, a secondary monochromator with Cu-Kα radiation (λ =1.5418 Å) and a PIXcel solid state detector (active length in 2θ 3.347°). Data were obtained from 2θ = 5 to 75° (step size 0.026 and time per step 80 s) at room temperature. A fixed divergence and antiscattering slit

were used to provide a constant volume of sample illumination. In order to calculate crystallinity index, Segal equation (Segal et al., 1959) was used:

$$\text{Crystallinity index (\%)} = ((I_{200} - I_{am}) / I_{200}) \times 100 \quad (1)$$

where I_{200} corresponds to the intensity of crystalline peak and I_{am} is referred to the intensity of the amorphous peak.

2.2.5. Atomic force microscopy (AFM)

AFM in tapping mode was used to characterize the morphology of the cellulose nanofibers, using a Nanoscope III scanning probe microscope (Multimode TM Digital instruments) with an integrated force generated by cantilever/silicon probes, applying a resonance frequency of about 180 kHz. The cantilever had a tip radius of 5–10 nm and was 125 nm long. CNF samples were prepared by spin-coating technique using Spin-coater P6700 at 2000 rpm for 120 s. A droplet from a CNF suspension of 0.01 wt% was deposited on mica substrates.

2.2.6. Rheological measurements

Rheological behavior of the prepared A-CNF and A-CNF-cur bioinks formulations was analyzed by flow viscosity, oscillatory shear stress sweep and structure recovery tests, using a Haake Viscotester Rheometer. Plate-plate geometry (35 mm) was used with a gap of 1 mm at 25 °C. Viscosity measurements were performed under steady shear rate from 0.2–100 s^{-1}. All samples were equilibrated for 40 s at 0.2 s^{-1} before each measurement. Experimental results of viscosity test were adjusted to Power-law model described with the following equation:

$$\eta = K \cdot (\dot{\gamma})^{n-1} \quad (2)$$

where η is the viscosity of the bioink measured in Pa·s, K is the consistency coefficient (Pa·s), $\dot{\gamma}$ is the shear rate measured in s^{-1} and n is the Power-law index.

Oscillatory stress sweep tests (in the Linear Viscoelastic Range (LVR)) were performed at 1 Hz in a shear stress range from 10 to 1000 Pa. For structure recovery tests, samples were subjected to a test consisting on the application of three consecutive shear rates of 0.2, 100 and 0.2 s^{-1} for 100 s each one. The recovery percentage was calculated from the ratio of viscosity values measured at 0.2 s^{-1} at the end and at the beginning of the assay, respectively. Oscillatory shear strain and frequency sweep measurements were performed using a TA Instruments ARES rheometer. Plate-plate geometry (25 mm) was used with a gap of 1.5 mm. Both assays were performed between 25−28 °C. For LVR determination, strain sweep tests were performed at 1 Hz from 0.01 to 100% of strain. Frequency sweep tests were performed at 1% of strain from 0.1 to 200 Hz. All experiments were performed in triplicate.

2.2.7. Scanning electron microscopy (SEM)

Morphology of freeze-dried scaffolds was analyzed by SEM, using a FEI ESEM Quanta 200 microscope operating at 5−20 kV. Surface and cross-section, perpendicular to layer deposition of the A-CNF freeze-dried scaffolds, were analyzed by irradiation with a high-energy electron beam. Samples were cut with a scalpel and then fixed on a carbon tape.

2.2.8. Compressive mechanical tests

The mechanical properties of the A-CNF scaffolds were evaluated by compressive tests. Five freeze-dried printed cylinders of 15 mm in diameter and 10 mm in height prepared from each bioink were compressed using an INSTRON 5967 with a load cell of 30 kN at a rate of 5 mm min^{-1}. All tests were performed up to 80 % of strain. The compressive modulus, calculated from the slope of the stress-strain curve in the elastic region, compressive strength, as the stress value at the compressive yield point, and densification strain, as the strain value at the intersection point between the lines of stress plateau and densification were collected from stress-stain curves and reported as mean value and standard deviations.

2.2.9. Swelling behavior

Swelling degree was studied by a general gravimetric method. Eighteen freeze-dried cylindrical scaffolds from each formulation A-CNF3, A-CNF4 and A-CNF5 (15 mm in diameter and 5 mm in height) were introduced in PBS solution (pH 7.4) at 37 °C with a constant stirring of 130 rpm. After that, swelling behavior was evaluated by weighting swollen samples at different time intervals of 30 min, 1, 2, 4, 6, and 24 h. Three samples from each time interval were tested to check the repeatability of the analysis. Swelling degree (SD) was calculated as follows:

$$\text{SD (\%)} = ((Ws - Wi) / Wi) \times 100 \quad (3)$$

where Ws represents the weight of swollen samples and Wi represents the weight of initial freeze-dried scaffold. Equilibrium was considered at 24 h.

The swollen samples were then freeze-dried and weighted again in order to calculate the disintegration rate of the scaffolds along the experiment, following the next equation:

$$\text{Disintegration rate (\%)} = 100 - ((Wd / Wi) \times 100) \quad (4)$$

where Wd is the weight of the freeze-dried samples at different times and Wi is the initial weight.

2.2.10. Preliminary cellular behavior

HEK293 T cells were a kind gift of Dra. María Muñoz Caffarel. Cells at passage 4 were defrosted and expanded by trypsinization, counting and replacement the culture medium composed by DMEM + 10 % FBS medium supplemented with 1% (w/v) L-glutamine and penicillin–streptomycin (100 IU mL^{-1}), every three days. A-CNF3 (n = 3), A-CNF4 (n = 3) and A-CNF5 (n = 3) freeze-dried cylindrical scaffolds of 15 mm diameter and 10 mm height were employed for this experiment. Scaffolds sterilization was carried out by UV light inside a laminar flow hood for 3 h, with no evidence of scaffold damage after the procedure. Fischbach et al. (2001) reported that the use of UV is appropriate for biomaterial sterilization for no longer than 5 h. Sterilized scaffolds were transferred in 24 well plate afterwards and then, 20000 cells at passage 15 were seeded in each well containing the scaffolds and the cell culture medium. Furthermore, 20000 cells were seeded in an empty well (without scaffold) as a control. The well plate with the seeded scaffolds and the control were stored for one week in the incubator at 37 °C in 5% CO_2 for cell growth, replacing the culture medium every 3 days and monitoring their presence by optical microscopy. After 7 days of incubation, cells were dyed with DAPI solution (5 mg mL^{-1}) diluted in PBS (1:2000) after washing each scaffold with PBS three times. DAPI-stained cells were observed after 5 min of incubation using a Zeiss LSM 710 confocal laser scanning microscope. The presence of cells were evaluated in fluorescence at the range of blue and green light spectra (λ = 400–550 nm), performing a multilayer analysis from the base to the surface of the seeded scaffolds.

2.2.11. In vitro curcumin release test and scaffold disintegration

Freeze-dried printed patches of A-CNF-cur (n = 3) with 25 × 25 × 4 mm^3 (length × width × height) were weighted and then soaked in 40 mL of PBS solution (pH 7.4) at 37 °C with constant stirring for 24 h. The released curcumin was evaluated based on proposed protocol by Sanoj Rejinold et al. (2011). In brief, at predetermined times, PBS was completely withdrawn and centrifuged for 30 min at 14000 rpm. PBS was dismissed whereas the pellet containing biopolymer and curcumin was resuspended in 15 mL of ethanol. The amount of released curcumin was determined at room temperature by UV–vis-NIR (Shimadzu 3600), comparing the absorbance at λ=426 nm (maximum absorbance of curcumin), with a standard curve previously prepared with known concentrations of curcumin (from 0 to

0.025 mg mL^{-1}) dissolved in ethanol, calculated as follows (Guaresti et al., 2017):

$$\text{Drug release } (\%) = (\text{Mr} / \text{Mt}) \times 100 \quad (5)$$

where Mr is the amount of curcumin released at different times and Mt is the total amount of curcumin loaded in the printed scaffold.

Considering that curcumin is completely soluble in ethanol whereas A-CNF tend to precipitate, curcumin-biopolymer-ethanol solutions of each sample were stored to quantify the amount of disintegrated A-CNF from the printed part. With that purpose, the solution was centrifuged for 30 min at 14000 rpm in order to collect them separately (precipitated), which were dried and weighted, and then compared to the initial weight of the scaffold, following Eq. (4) previously described.

3. Results and discussion

3.1. Materials characterization

The chemical and crystalline structures as well as the morphology of the employed CNF were analyzed by FTIR, XRD and AFM (Supplementary Fig. S1). FTIR spectrum showed the typical absorption bands of cellulose I pattern (Abidi et al., 2014) (Fig. S1A). Bands at 3375 and 3333 cm^{-1} corresponded to the stretching vibration of the hydrogen bonded hydroxyl groups, the bands in the 2900-2800 cm^{-1} interval were assigned to the C–H stretching vibration and the band around 1428 cm^{-1} to the CH_2 bending vibration. The band at 1641 cm^{-1} was associated to the absorbed water. The bands located at 1160 and 1031 cm^{-1} were attributed to C—O—C and C—O stretching vibrations of the glycosidic bonds, respectively. Finally, the band at 897 cm^{-1} was also attributed to the β-glycosidic linkage of cellulose structure (Li et al., 2014; Thiripura Sundari & Ramesh, 2012).

The XRD pattern of CNF showed strong diffraction peaks at $2\theta = 14.5°$, 16.5° and 23°, and a small peak at $2\theta = 34°$ (Fig. S1B), assigned respectively to $(1\bar{1}0)$, (110), (200) and (004) crystallographic planes, associated to the cellulose I crystalline structure (Gong et al., 2017). A crystallinity index of 71 % was estimated following the equation proposed by Segal et al. Morphological characteristics and dimensions of CNF were studied by AFM (Fig. S1C). As it could be observed, height and phase images showed nanofibers with several micrometers in length and diameters between 50−200 nm.

The chemical structure of SA, curcumin, and A-CNF and A-CNF-cur bioinks were also analyzed by FTIR (Fig. S2). SA spectrum showed in the 3400-3200 cm^{-1} interval the stretching vibration of hydrogen bonded O—H groups, and at 2924 cm^{-1} the stretching vibration of C–H. The bands located at 1600 and 1410 cm^{-1} corresponded to O═C—O- ion salt symmetric and asymmetric stretching vibrations and the band at 1043 cm^{-1} to the C—O stretching vibration. Finally, the bands at 950 cm^{-1} and 887 cm^{-1} correspond to C–H stretching vibrations from mannuronic and guluronic groups, respectively (Daemi & Barikani, 2012; Sarmento et al., 2006). Curcumin spectrum revealed a narrow band at 3510 cm^{-1}, corresponding to the phenolic O—H stretching vibration. The bands at 1626 cm^{-1} and 1600 cm^{-1} belonged to C═C groups and benzene rings vibrations. The bands located at 1510, 1435 and 1285 cm^{-1} were related to C═O and C═C characteristics vibrations, olefinic C–H bending vibrations and C—O stretching vibrations of aromatic rings, respectively. Finally, bands at 1027 and 840 cm^{-1} attributed to C—O—C stretching vibrations were found (Chen et al., 2015; Yallapu et al., 2010).

A-CNF spectrum presented typical bands of SA and cellulose, demonstrating the presence of both materials in the bioink formulations. Spectra of A-CNF and A-CNF-cur were compared, and small peaks at 1626 cm^{-1} and at 1510 cm^{-1} also observed in curcumin spectrum, were found in A-CNF-cur. Other bands were found in this bioink at 1285 cm^{-1} and 840 cm^{-1} corresponding to C—O stretching vibrations from aromatic rings of curcumin and C—O—C stretching vibrations, respectively; and thus demonstrating that curcumin was successfully integrated in the A-CNF biopolymer matrix.

3.2. Rheological characterization of A-CNF bioinks

With the aim of determining both the printability and shape fidelity of the prepared bioinks, rheological characterization was performed. As it could be observed in the flow viscosity curves (Fig. 1A), bioinks presented shear-thinning behavior in all cases, being the viscosity value at zero shear rate as well as the shear-thinning behavior, higher with increasing CNF content (Table 1). Shear-thinning is a typical behavior from non-Newtonian fluids and this could be demonstrated adjusting the experimental flow viscosity values to a Power-law model (Chen et al., 2019; Li et al., 2016). Power-law equation described in experimental section was used to calculate Power-law index (n), consistency coefficient (K) and Pearson correlation coefficient (R^2) for all bioink formulations, and then data were collected in Table 1. It was shown that n values approached to zero and K values raised as the CNF content increased, indicating non-Newtonian fluid characteristics and rise of shear-thinning behavior (Chen et al., 2019; Li et al., 2016; Liu et al., 2018). R^2 values close to 1 showed a strong correlation among experimental data of viscosity versus shear rate and the Power-law model. All this information also demonstrates that an increase in CNF content in the formulations produced an enhancement of shear-thinning behavior and non-Newtonian fluid characteristics in the developed bioinks.

The linear viscoelastic region (LVR) of the material was determined by means of strain sweep test (Fig. 1B). At strains values between 0.1 and 1%, the storage (G') and loss modulus (G'') were found to be independent of the strain amplitude, and G' was higher than G'' indicating a highly structured gel network in the LVR domain. At higher strain values, a drop in G' and G'' indicated permanent deformation and gel structure loss, resulting G'' higher than G'. Furthermore, it is known that G' defined the resistance of a material to be elastically deformed, and, thus, elastic solid-like behavior and mechanical strength (Chen et al., 2019; Liu et al., 2018). G' values at a strain of 0.1 % were collected in Table 1, showing a significant increment as the CNF content increased, and consequently indicating a rise of elasticity and strength properties of the bioinks.

Fig. 1C showed G' and G'' as a function of the applied shear stress. As it could be observed, for A-CNF1, G'' was always above G' indicating a liquid-like behavior of the material in the entire studied interval. For the rest of the bioinks G' was higher than G'' indicating solid-like behavior. The crossover of G' and G'' (when G'=G''), was denominated as yield stress (Feilden et al., 2016; Wilson et al., 2017), and it was reported by Chen et al. (2019) that is the minimum force needed for the extrusion of the material through the nozzle. The obtained yield stress values were summarized in Table 1. As it could be appreciated, the yield stress was higher as CNF content increased revealing that the higher CNF content was presented in the formulation the higher force will be needed to extrude the material.

Structure recovery test were performed to measure the recovery degree of the prepared bioinks, simulating printing conditions (Fig. 1D). For ideal bioinks, when shear rate increases, viscosity should drop and when it decreases or is completely removed, initial viscosity should be rapidly recovered (Abouzeid et al., 2018). Recovery percentage was calculated and it was also summarized in Table 1.

The obtained results indicated that, in general, recovery ability increased with the amount of CNF. In the case of the highest CNF content, the unexpected slightly lower recovery value could be caused by the partial loss of material during the assay at the maximum shear rate. Nevertheless, the viscosity reached when the shear rate application stopped was enough to support the shape of printed scaffolds.

In Fig. 1E, frequency sweep tests for the different bioinks were presented. In general, G' and G'' presented marked frequency dependency and the two modulus increased notably as the oscillation frequency did. The non-covalent character of the hydrogen bonding interactions

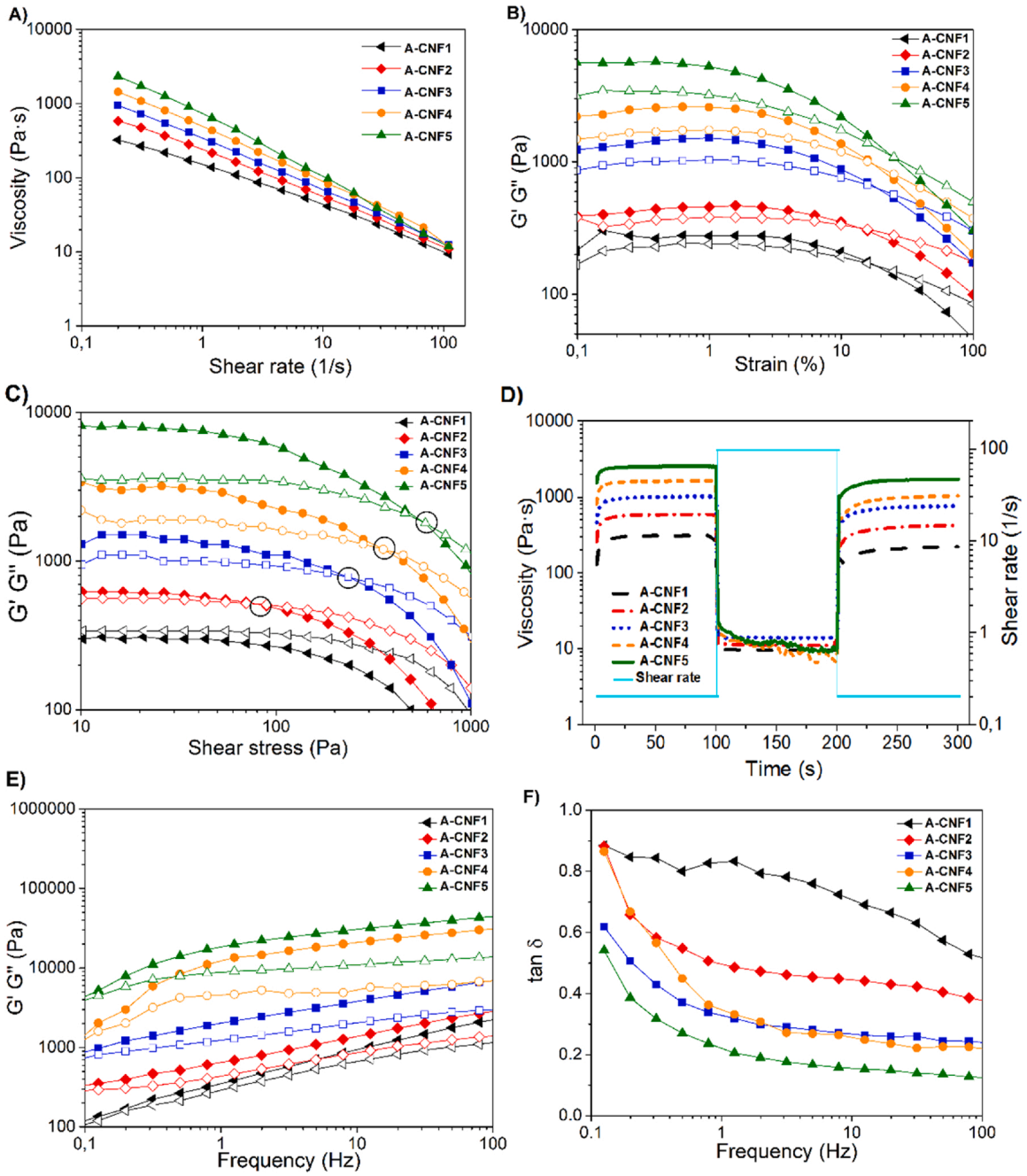

Fig. 1. Rheological data from the different bioink formulations: A) Steady-state viscosity as a function of shear rate. B) G' (solid symbols) and G'' (open symbols) as a function of shear strain. C) G' (solid symbols) and G'' (open symbols) as a function of shear stress. D) Structure recovery test. E) G' (solid symbols) and G'' (open symbols) as a function of frequency. F) Tan δ values as a function of frequency.

Table 1
Viscosity at zero shear rate, G' at strain of 0.1 %, yield stress and recovery percentage of the five bioinks.

Bioink	Viscosity (Pa·s)	n	K	R^2	G' (Pa)	Yield stress (Pa)	Recovery (%)
A-CNF1	290 ± 32	0.4386	149.15	0.994	277 ± 51	–	72 ± 2
A-CNF2	518 ± 59	0.3617	234.8	0.995	463 ± 55	90 ± 12	72 ± 1
A-CNF3	850 ± 93	0.3081	333.44	0.998	1233 ± 76	284 ± 46	75 ± 3
A-CNF4	1418 ± 71	0.2566	481.37	0.997	2177 ± 68	365 ± 16	65 ± 6
A-CNF5	2266 ± 99	0.1453	697.53	0.993	5583 ± 76	600 ± 21	66 ± 3

existing between the alginate and the nanocelullose led to this rheological pattern, as reported by Liu et al. (2019). As it could also be observed, bioinks with higher modulus values corresponded to those with larger CNF content. Furthermore, it was known that the larger difference between G' and G'' values indicates highly organized gel-like structure whereas similar values indicates poor elastic behavior and weakly organized network structure of the material (Abouzeid et al., 2018; Liu et al., 2019), as could be observed for the A-CNF1 bioink. As it

could be noticed, the existing gap between the two dynamic modulus increased with the applied frequency, reaching its maximum value at the highest frequency, where the solid character of the viscoelastic bioink predominated.

Ideal bioink formulations also needs good solid-liquid balance to be successfully printed, with good interconnection between layers and correct structure fidelity. As it is well known, the ratio between G'' and G' (G''/G') can be correlated with shape strength and internal network structure, which is determined as tan δ (Gao et al., 2018; Liu et al., 2018). Values close to 0 indicates solid and elastic behavior, and values close to 1 indicates more liquid-like behavior (Abouzeid et al., 2018; Gao et al., 2018). Gao et al. (2018) reported that alginate-based bioinks with tan δ values between 0.25 and 0.45 presented good smoothness and structural integrity. Tan δ results from frequency sweep test of the developed bioinks are shown in Fig. 1F and the obtained results revealed adequate tan δ values for the bioinks with higher CNF content, whereas undesirable values higher than 0.5 where obtained for the two formulations with lower CNF content, A-CNF1 and A-CNF2.

3.3. 3D printing of A-CNF bioinks

All prepared A-CNF bioinks were 3D printed in several forms (Fig. 2) in order to correlate the measured rheological parameters and printing performance. All developed bioinks presented suitable extrudability through the nozzle, filament formation and correct layer deposition, but, as it could be observed, printed samples from A-CNF1 and A-CNF2 bioinks did not present accurate reproduction of the dog-bone shape, provided in the computer-aided design (CAD) model. A-CNF3, A-CNF4 and A-CNF5 showed shape fidelity and accuracy, structural integrity, smooth uniformity and good connection between layers after printing.

Viscoelastic capacity of the bioinks is crucial to overcome shape fidelity issues, as it has been mentioned before. High G' values at low shear strains were related to the presence of a highly structured network, but after the application of a shear force as happens during 3D printing, materials must be able to recover almost the initial G' values, demonstrating that the physical network was restored (Chen et al., 2019). Printed samples of A-CNF formulations with lower CNF content did not show suitable shape retention (Fig. 2) and the initial G' values up to 463 Pa (Table 1), demonstrating that 1 and 2 % of CNF content into a SA solution were not enough to guarantee shape fidelity and suitable viscoelastic characteristics for 3D printing. For A-CNF3, A-CNF4 and A-CNF5 bioinks initial G' values beyond 1200 Pa denoted the presence of a highly strength network that ensured shape fidelity after printing. Bendtsen et al. (2017) reported values of G' among 600 and 1200 Pa for high accuracy and shape fidelity of alginate-based bioinks, whereas Chen et al. (2019) reported initial G' values among 1150 and 6909 Pa for correct shape retention and resolution in starch-based bioinks. The deficient shape strength and structural fidelity of the A-CNF1 and A-CNF2 bioinks were also closely related to the measured low viscosity values at zero shear rate and yield stress, as well as fluidity and liquid-like behavior above discussed.

In view of the results, it might be concluded that formulations with CNF content of at least 3 wt% presented suitable viscoelastic characteristics to be successfully printed. The printed samples reproduced more accurately the CAD model as the CNF content increased in the A-CNF bioink formulations. The CNF acted as effective rheological modifier rising shape fidelity, structural integrity and avoiding collapse of printed samples, also in agreement with that reported by Leppiniemi et al. (2017) and Heggset et al. (2019). Therefore, formulations of A-CNF3, A-CNF4 and A-CNF5 were selected for 3D printing of cylindrical samples and preparation of porous scaffolds after convenient freeze-drying, whereas A-CNF1 and A-CNF2 formulations were discarded for the next experiments.

3.4. Morphological and mechanical characterization of A-CNF scaffolds

The morphology of printed scaffolds was analyzed by SEM. Images of freeze-dried scaffolds of A-CNF3, A-CNF4 and A-CNF5 were obtained in both surface and in the cross-section perpendicular to the deposition of the layers. As can be observed, surface morphology of A-CNF3 scaffold presented larger porosity (upper Fig. 3A) than A-CNF4 and A-CNF5, where non–homogeneous surfaces were observed, with compact and porous regions appearing together (upper Fig. 3B and C, respectively). In cross-section images (Fig. 3, down images), decreased porosity and higher compactness were observed as the CNF content increased. As it could be noticed in the images, the different layers were correctly merged during the printing process and no separated threads delimiting each layer were observed. Indeed, the scaffolds appeared as a single block, demonstrating extrusion uniformity of the material and correct deposition and support of the different layers.

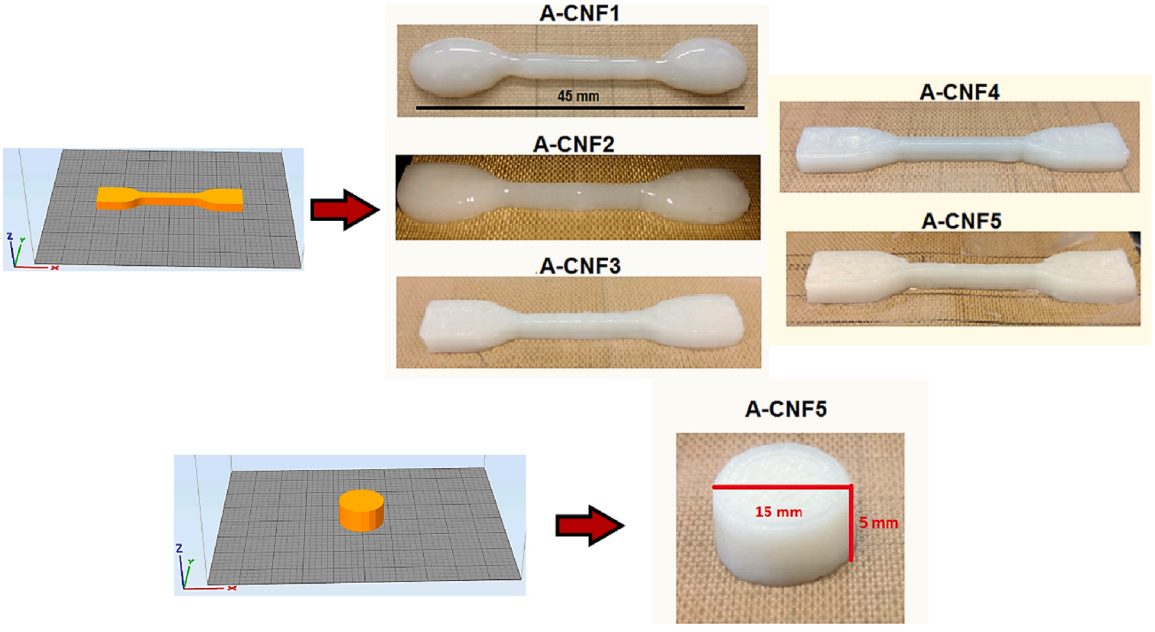

Fig. 2. Computer-aided design (CAD) models and digital images of 3D printed dog-bone and cylindrical samples of developed A-CNF bioinks.

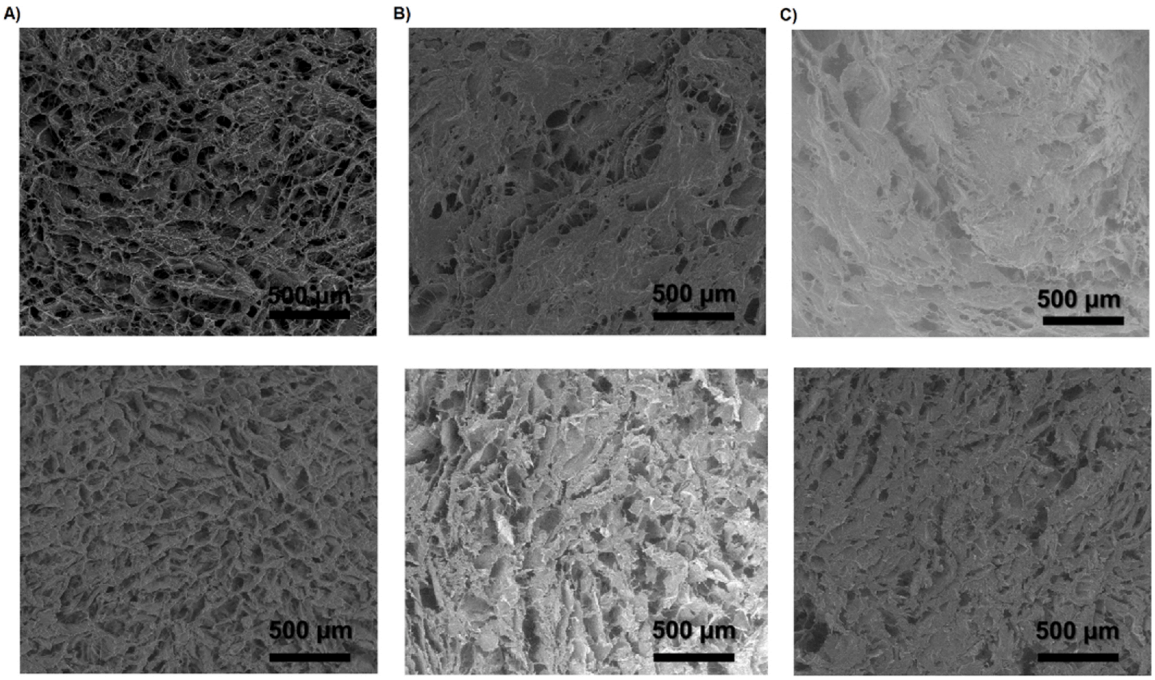

Fig. 3. Scanning electron microscopy (SEM) images of A-CNF freeze-dried scaffolds. Composition: A) A-CNF3, B) A-CNF4 and C) A-CNF5. Upper images represent surface and down images represent cross-section.

Freeze-drying consists on removing water from the printed scaffolds by sublimation, obtaining a porous matrix. Consequently, the ratio of solid content and the amount of water in the bioink formulations control the final porosity, increasing as the solid content decreases (Wu et al., 2010). Thus, the higher solid content of the formulations with larger amount of CNF led to reduced porosity both in the surface and within the inner part of the scaffolds. It is worthy to note that varying the CNF content only in 1 wt% was enough to clearly observe changes in morphology, porosity and compactness between the three different printed scaffolds.

Compressive mechanical stress-strain curves of the freeze-dried cylindrical printed scaffolds from A-CNF3, A-CNF4 and A-CNF5 were shown in Fig. 4. Compressive modulus, compressive stress and densification strain values obtained from the curves were summarized in Table 2. All samples followed the typical compression behavior of porous materials, showing the linear elastic behavior at low stress values, followed by an extended plateau and a final densification region, where the stress dramatically increased.

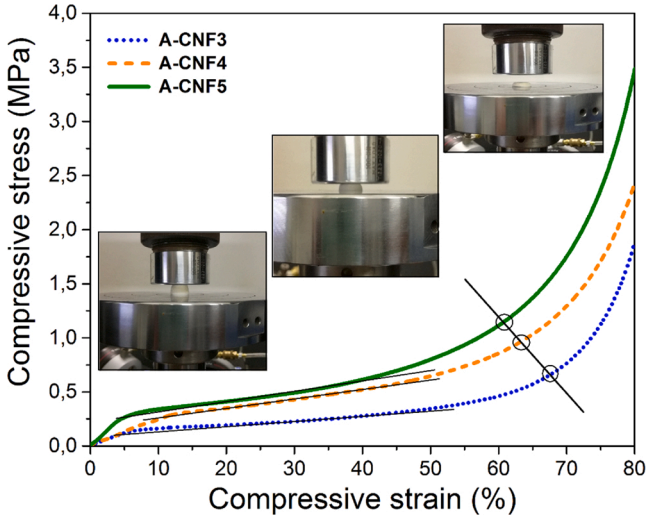

Fig. 4. Compressive stress-strain curves of A-CNF3, A-CNF4 and A-CNF5 freeze-dried scaffolds.

Table 2
Compressive properties of freeze-dried A-CNF scaffolds.

Scaffold	Young's modulus (MPa)	Compressive strength (MPa)	Densification strain (%)
A-CNF3	12.0 ± 5.7	1.5 ± 0.4	66.6 ± 2.1
A-CNF4	22.8 ± 12.3	2.7 ± 0.8	65.6 ± 1.3
A-CNF5	28.1 ± 13.4	3.2 ± 0.8	63.0 ± 1.2

Scaffolds with higher CNF content showed higher mechanical strength and stiffness, attributed to the reinforcing effect of CNF in good agreement with the previous rheological results. In fact, results showed increasing Young's modulus and compressive stress values as CNF content of scaffolds increased, while the densification strain decreased due to the reduction in the porosity of the scaffold. A-CNF3 showed significantly lower modulus and compressive strength than A-CNF4 and A-CNF5, whereas the latter reached non-porous behavior faster than A-CNF3 and A-CNF4.

3.5. Swelling degree of A-CNF scaffolds

Swelling degree and disintegration rate of A-CNF freeze-dried scaffolds was evaluated for 24 h and the obtained results were shown in Fig. 5. Swelling capacity was higher in A-CNF3 scaffolds than A-CNF4 and A-CNF5 (Fig. 5A). This could be attributed to the previously observed higher porosity in the A-CNF3 that enabled faster water penetration into the scaffolds, compared to those with higher CNF content. Guaresti et al. (2017) and Mirzaei et al. (2013) reported similar swelling degree values for natural polymer based freeze-dried hydrogels. In this experiment, it should be taken into account that both the mass gain due to the water uptake and the mass loss were competing, especially from the 4^{th} hour due to the progressive disintegration of the scaffolds in the PBS solution. The faster water uptake into the scaffolds with higher porosity and less CNF content resulted in higher percentage

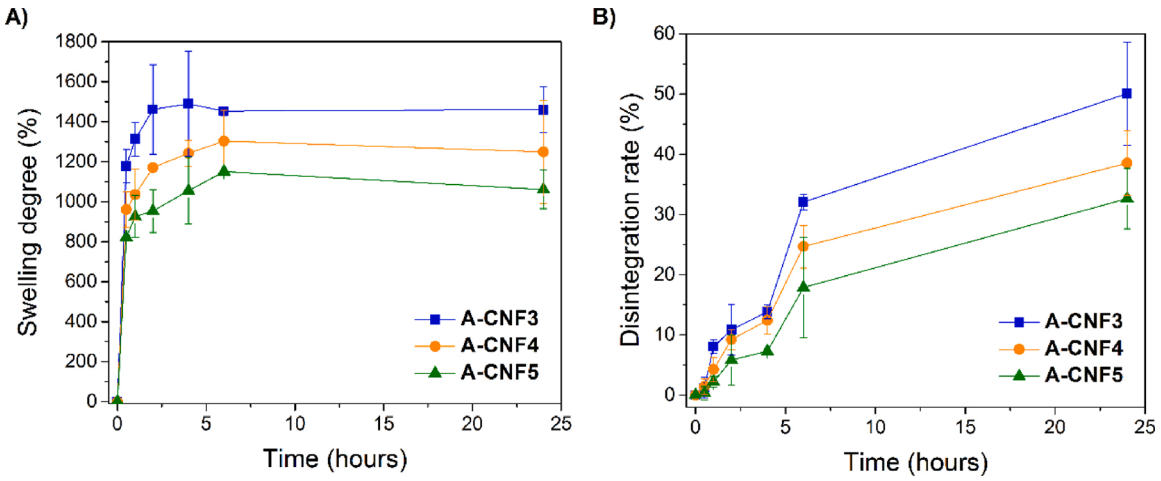

Fig. 5. A) Swelling degree and B) disintegration rate of A-CNF freeze-dried scaffolds.

of scaffold disintegration over time, as it was observed in Fig. 5B.

3.6. Preliminary cellular behavior in A-CNF scaffolds

Preliminary qualitative analysis of cell presence was performed to test the biocompatible character of the developed A-CNF scaffolds. HEK293 T cell line was seeded in freeze-dried A-CNF3, A-CNF4 and A-CNF5 scaffolds, and then they were stored for one week in the incubator, at 37 °C. After that time soaked in culture media, it was observed that none of the scaffolds lost totally the structure integrity. The nucleus of the cells were dyed with DAPI before the qualitative analysis and then, seeded scaffolds were evaluated through a multilayer analysis by confocal laser scanning microscopy, taking images of the scaffolds layer by layer throughout the z-axis at different heights, from the base to the surface, as it has been indicated in Fig. 6. As could be observed in the control image, seeded cells appeared as fluorescence stained circles whereas in the images from the seeded A-CNF3 scaffold, both the cells and the CNF were detected. Khalid et al. (2019) reported that cellulose nanofibers can be detected in the confocal laser microscope in blue and green fluorescence emission spectra, and consequently they were observed as fibers shape in the images, especially in those referred to the middle part and the surface of the scaffold. Comparing the images taken from the scaffold to that obtained for the control, it could be appreciated that both cells and CNF were observed in the A-CNF3 scaffold, revealing that these cells could integrate throughout the porous matrix of the A-CNF scaffolds.

3.7. Preparation and 3D printing of A-CNF-cur bioinks

The suitability of the prepared A-CNF scaffolds as platforms for local drug administration was evaluated. Curcumin was chosen due to its recent interest in the treatment of cancer and inflammatory diseases

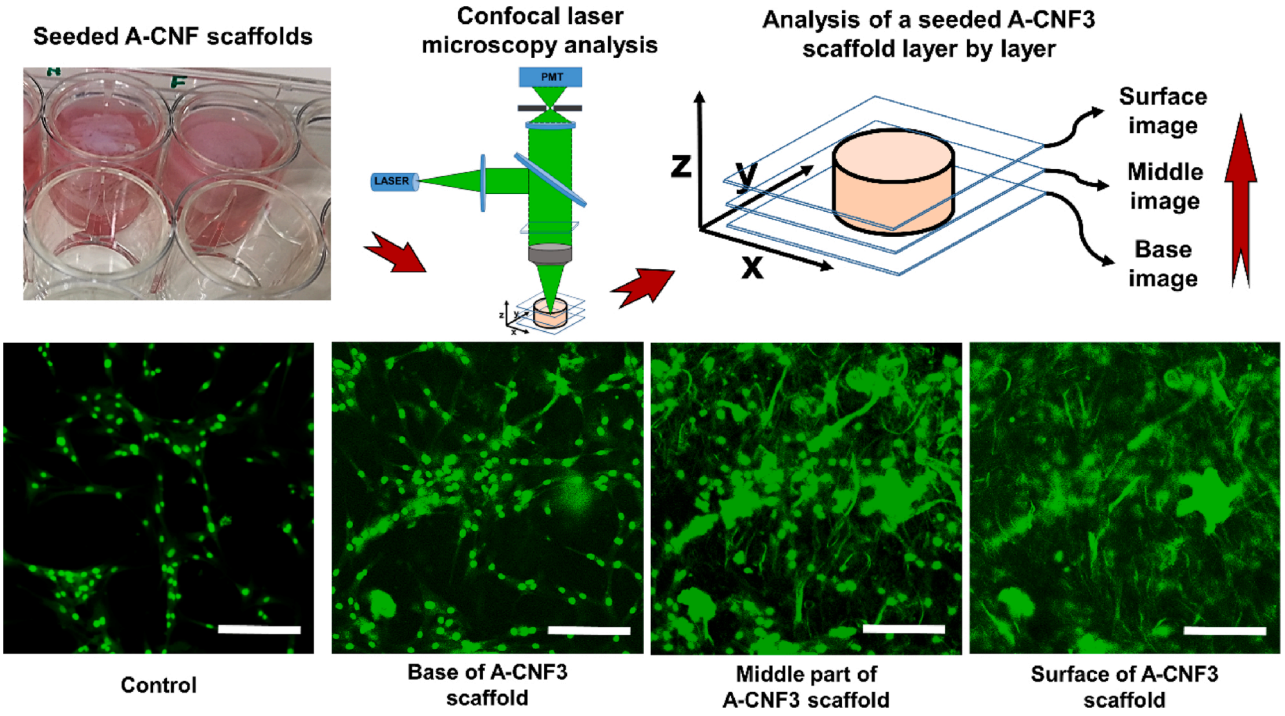

Fig. 6. Preliminary cellular behavior in A-CNF scaffolds. Images of the upper part represent the seeded A-CNF scaffolds in a well plate after one week of growth and subsequent multilayer analysis by confocal laser microscopy. Down images represent the control and a seeded A-CNF3 scaffold taken layer by layer from the base to the surface by confocal laser microscopy in green fluorescence emission spectrum. Scale bars represent 100 μm.

(Doello et al., 2018; Farhood et al., 2019). Hydrophobic curcumin showed low solubility in water or in PBS (Fig. 7A) but it could be stabilized in alginate aqueous solutions (Fig. 7B). When curcumin is added to the alginate solution, hydrophobic particles are trapped and stabilized by polymeric chains and they stay homogeneously distributed throughout the aqueous alginate matrix despite their low solubility. Moreover, CNF could even improve this stabilization, as it was reported by Li et al. (2013).

Thus, curcumin was added to A-CNF3, A-CNF4 and A-CNF5 bioinks and then they were successfully 3D printed in a patch shape configured by CAD (Fig. 7C), showing that printed samples were able to remain the shape previously designed. It was also shown that curcumin was homogeneously integrated and stabilized in the A-CNF bioinks, as was already demonstrated by FTIR analysis. As it could be observed, the addition of curcumin did not change the properties of the A-CNF bioinks during printing process, showing good printability, shape fidelity and stiffness of the printed patches, as those without drug. Finally, printed patches were freeze-dried.

3.8. *In vitro curcumin release from A-CNF-cur patches*

3D printed A-CNF-cur patches were evaluated as drug delivery systems. Freeze-dried patches were assessed *in vitro* conditions (PBS, 37 °C) for 24 h, and the amount of released curcumin was determined by UV–vis spectroscopy.

As it could be observed in Fig. 8A, A-CNF3-cur and A-CNF4-cur patches showed shortest time of total curcumin release, which was estimated to be around 6 h. Curcumin release in A-CNF5-cur patches was measured for 24 h, and the results showed that only 50 % of the total amount of curcumin was released at that time. Due to the low solubility of this molecule in PBS, the release of curcumin will be triggered by the water entry into the porous scaffold and its progressive disintegration. Thus, curcumin release was dependent on the previous stabilization of this hydrophobic molecule in A-CNF biopolymer matrix, the swelling capacity of A-CNF-cur scaffolds and its progressive disintegration. For that reason, A-CNF-cur scaffold disintegration rate was also simultaneously monitored (Fig. 8B), collecting the residual A-CNF biopolymer at predetermined times (Fig. 8C). A-CNF3-cur and A-CNF4-cur showed faster scaffold disintegration than A-CNF5-cur, in correlation with curcumin release curves. Regarding the effect of the CNF amount in the different A-CNF-cur printed patches, it has already been demonstrated in those without drug that higher content of CNF reduced porosity and increased stiffness of the printed scaffolds, giving rise to a slower water entry into the scaffold and, consequently, lower disintegration rate. For that reason, curcumin release and scaffold disintegration of A-CNF5-cur patches was slower than in A-CNF3-cur and A-CNF4-cur.

4. Conclusions

In this study, different formulations of alginate-cellulose nanofibers (A-CNF) were developed to be used as bioinks for 3D printing. Rheological tests were performed to give an overview of their printability. All bioink formulations showed shear thinning behavior, but only A-CNF3, A-CNF4 and A-CNF5 presented suitable conditions, shape fidelity and high accuracy after printing, that is, good solid-liquid balance which involves good interconnection between layers and correct structure retention. The increment of CNF content in the formulations provided viscoelastic capacity to the bioinks, which was translated into good printability and shape fidelity after 3D printing of A-CNF3, A-CNF4 and A-CNF5 formulations. The scaffolds prepared by freeze-drying showed an increment of compressive modulus and structure compactness as the CNF amount increased, while the swelling capacity and disintegration rate of the scaffolds were found to decrease due to the reduction of the porosity. In order to evaluate the capacity of the 3D printed scaffolds as drug delivery systems, curcumin was added to A-CNF selected formulations, obtaining bioinks suitable for 3D printing technology that guaranteed its structure stabilization and maintained shape fidelity after printing. A-CNF-cur bioinks were 3D printed in patch shape and freeze-dried. Curcumin release from scaffolds was evaluated *in vitro* conditions and results showed that the release was driven by the A-CNF-cur scaffold disintegration instead of by the dissolution of curcumin in PBS, due to the hydrophobicity of this molecule. Porous structure of freeze-dried patches allowed water entry due to its swelling capacity, triggering A-CNF-cur disintegration and curcumin release. An increment of CNF amount in 1 wt% between the suitable A-CNF3-cur, A-CNF4-cur and A-CNF5-cur bioink formulations was enough to guarantee a slower drug release due to the decreased porosity of the scaffold which finally involved a slower water uptake and slower disintegration rate of the scaffolds. These differences in the drug release kinetics can be used as a way to customize the drug delivery system, which could be adapted according to the patient necessities. Therefore, the three suitable A-CNF formulations for 3D printing technology could be employed as tailor-

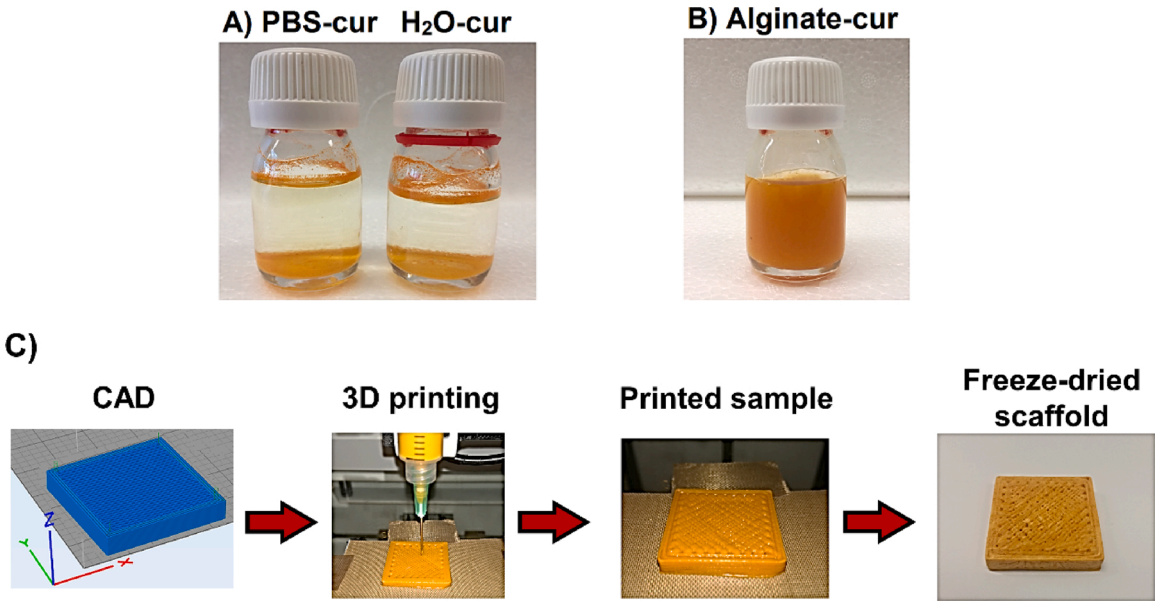

Fig. 7. A) Curcumin in PBS and water solutions. B) Curcumin stabilization in alginate aqueous solution (4 wt%). C) Process for obtaining an A-CNF4-cur patch.

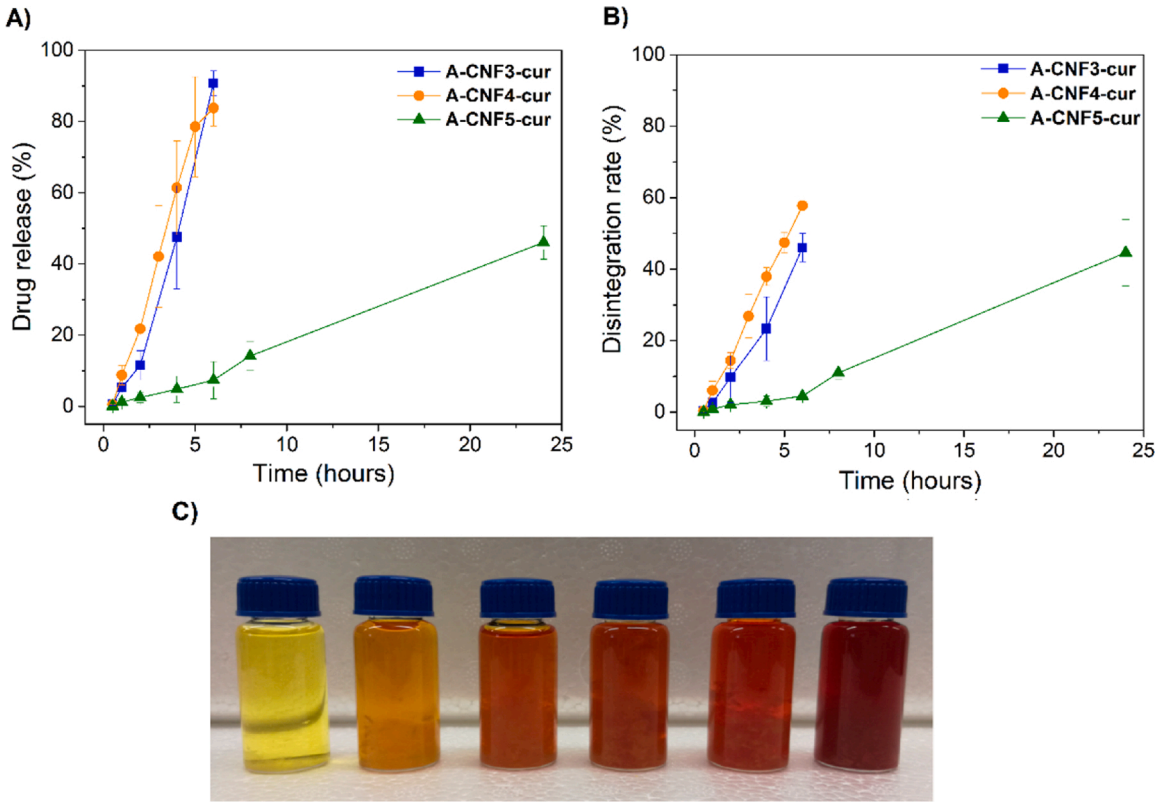

Fig. 8. A) Curcumin release curves from A-CNF-cur patches. B) Disintegration rate of A-CNF-cur patches. C) Images taken from A-CNF4-cur during release and disintegration process at times of 30 min, 1, 2, 3, 4, 5, and 6 h.

made drug delivery systems, adjusting specific patient drug dosage and requirements in the release form.

CRediT authorship contribution statement

Raquel Olmos-Juste: Methodology, Investigation, Writing, Visualization, Formal analysis. **Borja Alonso-Lerma:** Methodology, Investigation. **Raul Perez-Jimenez:** Methodology, Investigation. **Nagore Gabilondo:** Conceptualization, Methodology, Investigation, Supervision, Writing, Visualization, Formal analysis, Funding acquisition. **Arantxa Eceiza:** Conceptualization, Methodology, Investigation, Supervision, Writing, Visualization, Formal analysis, Funding acquisition.

Acknowledgments

Financial support from the University of the Basque Country (UPV/EHU) (GIU18/216 Research Group), from the Basque Government in the frame of Elkartek KK-2020/00053 and PIBA2020-1-0041 and from Spanish Ministry of Science, Innovation and Universities and European Union (MICINN/EU/FEDER) in the frame of MAT2016-76294-R and PID2019-105090RB-I00 projects, are gratefully acknowledged. Moreover, we are grateful to the Macrobehavior-Mesostructure-Nanotechnology SGIker unit of the UPV/EHU. Raquel Olmos Juste wishes to acknowledge the Ministry of Economy, Industry and Competitiveness for her PhD grant.

Appendix A. Supplementary data

Supplementary material related to this article can be found, in the online version, at doi:https://doi.org/10.1016/j.carbpol.2021.118026.

References

Abdelwahed, W., Degobert, G., Stainmesse, S., & Fessi, H. (2006). Freeze-drying of nanoparticles: Formulation, process and storage considerations. *Advanced Drug Delivery Reviews, 58*(15), 1688–1713. https://doi.org/10.1016/j.addr.2006.09.017

Abidi, N., Cabrales, L., & Haigler, C. H. (2014). Changes in the cell wall and cellulose content of developing cotton fibers investigated by FTIR spectroscopy. *Carbohydrate Polymers, 100*, 9–16. https://doi.org/10.1016/j.carbpol.2013.01.074

Abouzeid, R. E., Khiari, R., Beneventi, D., & Dufresne, A. (2018). Biomimetic mineralization of three-dimensional printed alginate/TEMPO-oxidized cellulose nanofibril scaffolds for bone tissue engineering. *Biomacromolecules, 19*(11), 4442–4452. https://doi.org/10.1021/acs.biomac.8b01325

Anagha, B., George, D., Maheswari, P. U., & Begum, K. M. M. S. (2019). Biomass derived antimicrobial hybrid cellulose hydrogel with green ZnO nanoparticles for curcumin delivery and its kinetic modelling. *Journal of Polymers and the Environment, 27*(9), 2054–2067. https://doi.org/10.1007/s10924-019-01495-y

Bendtsen, S. T., Quinnell, S. P., & Wei, M. (2017). Development of a novel alginate-polyvinyl alcohol-hydroxyapatite hydrogel for 3D bioprinting bone tissue engineered scaffolds. *Journal of Biomedical Materials Research - Part A, 105*(5), 1457–1468. https://doi.org/10.1002/jbm.a.36036

Buffiere, J., Balogh-Michels, Z., Borrega, M., Geiger, T., Zimmermann, T., & Sixta, H. (2017). The chemical-free production of nanocelluloses from microcrystalline cellulose and their use as Pickering emulsion stabilizer. *Carbohydrate Polymers, 178* (June), 48–56. https://doi.org/10.1016/j.carbpol.2017.09.028

Chen, H., Xie, F., Chen, L., & Zheng, B. (2019). Effect of rheological properties of potato, rice and corn starches on their hot-extrusion 3D printing behaviors. *Journal of Food Engineering, 244*(September 2018), 150–158. https://doi.org/10.1016/j.jfoodeng.2018.09.011

Chen, X., Zou, L. Q., Niu, J., Liu, W., Peng, S. F., & Liu, C. M. (2015). The stability, sustained release and cellular antioxidant activity of curcumin nanoliposomes. *Molecules, 20*(8), 14293–14311. https://doi.org/10.3390/molecules200814293

Daemi, H., & Barikani, M. (2012). Synthesis and characterization of calcium alginate nanoparticles, sodium homopolymannuronate salt and its calcium nanoparticles. *Scientia Iranica, 19*(6), 2023–2028. https://doi.org/10.1016/j.scient.2012.10.005

Dey, S., & Sreenivasan, K. (2014). Conjugation of curcumin onto alginate enhances aqueous solubility and stability of curcumin. *Carbohydrate Polymers, 99*, 499–507. https://doi.org/10.1016/j.carbpol.2013.08.067

Doello, K., Ortiz, R., Alvarez, P. J., Melguizo, C., Cabeza, L., & Prados, J. (2018). Latest in vitro and in vivo assay, clinical trials and patents in Cancer treatment using curcumin: A literature review. *Nutrition and Cancer, 70*(4), 569–578. https://doi.org/10.1080/01635581.2018.1464347

Farhood, B., Mortezaee, K., Goradel, N. H., Khanlarkhani, N., Salehi, E., Nashtaei, M. S., Najafi, M., & Sahebkar, A. (2019). Curcumin as an anti-inflammatory agent:

Implications to radiotherapy and chemotherapy. *Journal of Cellular Physiology, 234* (5), 5728–5740. https://doi.org/10.1002/jcp.27442
Feilden, E., Blanca, E. G. T., Giuliani, F., Saiz, E., & Vandeperre, L. (2016). Robocasting of structural ceramic parts with hydrogel inks. *Journal of the European Ceramic Society, 36*(10), 2525–2533. https://doi.org/10.1016/j.jeurceramsoc.2016.03.001
Fischbach, C., Tessmar, J., Lucke, A., Schnell, E., Schmeer, G., Blunk, T., & Göpferich, A. (2001). Does UV irradiation affect polymer properties relevant to tissue engineering? *Surface Science, 491*(3), 333–345. https://doi.org/10.1016/S0039-6028(01)01297-3
Gao, B., Yang, Q., Zhao, X., Jin, G., Ma, Y., & Xu, F. (2016). 4D bioprinting for biomedical applications. *Trends in Biotechnology, 34*(9), 746–756. https://doi.org/10.1016/j.tibtech.2016.03.004
Gao, T., Gillispie, G. J., Copus, J. S., Kumar, A. P. R., Seol, Y. J., Atala, A., Yoo, J. J., & Lee, S. J. (2018). Optimization of gelatin-alginate composite bioink printability using rheological parameters: A systematic approach. *Biofabrication, 10*(3), 34106. https://doi.org/10.1088/1758-5090/aacdc7
Gómez, H. C., Serpa, A., Velásquez-Cock, J., Gañán, P., Castro, C., Vélez, L., & Zuluaga, R. (2016). Vegetable nanocellulose in food science: A review. *Food Hydrocolloids, 57*, 178–186. https://doi.org/10.1016/j.foodhyd.2016.01.023
Gong, J., Li, J., Xu, J., Xiang, Z., & Mo, L. (2017). Research on cellulose nanocrystals produced from cellulose sources with various polymorphs. *RSC Advances, 7*(53), 33486–33493. https://doi.org/10.1039/c7ra06222b
Guaresti, O., García–Astrain, C., Palomares, T., Alonso–Varona, A., Eceiza, A., & Gabilondo, N. (2017). Synthesis and characterization of a biocompatible chitosan–based hydrogel cross–linked via 'click' chemistry for controlled drug release. *International Journal of Biological Macromolecules, 102*, 1–9. https://doi.org/10.1016/j.ijbiomac.2017.04.003
Heggset, E. B., Strand, B. L., Sundby, K. W., Simon, S., Chinga-Carrasco, G., & Syverud, K. (2019). Viscoelastic properties of nanocellulose based inks for 3D printing and mechanical properties of CNF/alginate biocomposite gels. *Cellulose, 26*(1), 581–595. https://doi.org/10.1007/s10570-018-2142-3
Hölzl, K., Lin, S., Tytgat, L., Van Vlierberghe, S., Gu, L., & Ovsianikov, A. (2016). Bioink properties before, during and after 3D bioprinting. *Biofabrication, 8*(3), 1–19. https://doi.org/10.1088/1758-5090/8/3/032002
Hossen, S., Hossain, M. K., Basher, M. K., Mia, M. N. H., Rahman, M. T., & Uddin, M. J. (2019). Smart nanocarrier-based drug delivery systems for cancer therapy and toxicity studies: A review. *Journal of Advanced Research, 15*, 1–18. https://doi.org/10.1016/j.jare.2018.06.005
Jia, J., Richards, D. J., Pollard, S., Tan, Y., Rodriguez, J., Visconti, R. P., Trusk, T. C., Yost, M. J., Yao, H., Markwald, R. R., & Mei, Y. (2014). Engineering alginate as bioink for bioprinting. *Acta Biomaterialia, 10*(10), 4323–4331. https://doi.org/10.1016/j.actbio.2014.06.034
Jose, R. R., Rodriguez, M. J., Dixon, T. A., Omenetto, F., & Kaplan, D. L. (2016). Evolution of bioinks and additive manufacturing technologies for 3D bioprinting. *ACS Biomaterials Science and Engineering, 2*(10), 1662–1678. https://doi.org/10.1021/acsbiomaterials.6b00088
Khalid, A., Zhang, L., Tetienne, J. P., Abraham, A. N., Poddar, A., Shukla, R., Shen, W., & Tomljenovic-Hanic, S. (2019). Intrinsic fluorescence from cellulose nanofibers and nanoparticles at cell friendly wavelengths. *APL Photonics, 4*(2), Article 020803. https://doi.org/10.1063/1.5079883
Khouri, S. J., & Buss, V. (2011). Interaction of cationic cyanine dye with algal alginates: Evidence for a polymer bound dye dimer. *Journal of Biophysical Chemistry, 2*(4), 380–385. https://doi.org/10.4236/jbpc.2011.24043
Kunnumakkara, A. B., Anand, P., & Aggarwal, B. B. (2008). Curcumin inhibits proliferation, invasion, angiogenesis and metastasis of different cancers through interaction with multiple cell signaling proteins. *Cancer Letters, 269*(2), 199–225. https://doi.org/10.1016/j.canlet.2008.03.009
Kyle, S., Jessop, Z. M., Al-Sabah, A., & Whitaker, I. S. (2017). 'Printability' of candidate biomaterials for extrusion based 3D printing: State-of-the-art. *Advanced Healthcare Materials, 6*(16), 1–16. https://doi.org/10.1002/adhm.201700264
Lee, M. J., Kim, S. E., Park, J., Ahn, G. Y., Yun, T. H., Choi, I., Kim, H. J., & Choi, S. W. (2019). Curcumin-loaded biodegradable polyurethane scaffolds modified with gelatin using 3D printing technology for cartilage tissue engineering. *Polymers for Advanced Technologies, 30*(12), 3083–3090. https://doi.org/10.1002/pat.4740
Leppiniemi, J., Lahtinen, P., Paajanen, A., Mahlberg, R., Metsä-Kortelainen, S., Pinomaa, T., Pajari, H., Vikholm-Lundin, I., Pursula, P., & Hytönen, V. P. (2017). 3D-printable bioactivated nanocellulose-alginate hydrogels. *ACS Applied Materials and Interfaces, 9*(26), 21959–21970. https://doi.org/10.1021/acsami.7b02756
Li, B., Konecke, S., Wegiel, L. A., Taylor, L. S., & Edgar, K. J. (2013). Both solubility and chemical stability of curcumin are enhanced by solid dispersion in cellulose derivative matrices. *Carbohydrate Polymers, 98*(1), 1108–1116. https://doi.org/10.1016/j.carbpol.2013.07.017
Li, H., Liu, S., & Li, L. (2016). Rheological study on 3D printability of alginate hydrogel and effect of graphene oxide. *International Journal of Bioprinting, 2*(2), 54–66. https://doi.org/10.18063/IJB.2016.02.007
Li, M., Wang, L. J., Li, D., Cheng, Y. L., & Adhikari, B. (2014). Preparation and characterization of cellulose nanofibers from de-pectinated sugar beet pulp. *Carbohydrate Polymers, 102*(1), 136–143. https://doi.org/10.1016/j.carbpol.2013.11.021
Liu, Y., Yu, Y., Liu, C., Regenstein, J. M., Liu, X., & Zhou, P. (2019). Rheological and mechanical behavior of milk protein composite gel for extrusion-based 3D food printing. *Lwt- Food Science and Technology, 102*(August 2018), 338–346. https://doi.org/10.1016/j.lwt.2018.12.053
Liu, Z., Zhang, M., Bhandari, B., & Yang, C. (2018). Impact of rheological properties of mashed potatoes on 3D printing. *Journal of Food Engineering, 220*, 76–82. https://doi.org/10.1016/j.jfoodeng.2017.04.017
Ma, J., Lin, Y., Chen, X., Zhao, B., & Zhang, J. (2014). Flow behavior, thixotropy and dynamical viscoelasticity of sodium alginate aqueous solutions. *Food Hydrocolloids, 38*, 119–128. https://doi.org/10.1016/j.foodhyd.2013.11.016
Maheshwari, R. K., Singh, A. K., Gaddipati, J., & Srimal, R. C. (2006). Multiple biological activities of curcumin: A short review. *Life Sciences, 78*(18), 2081–2087. https://doi.org/10.1016/j.lfs.2005.12.007
Markstedt, K., Mantas, A., Tournier, I., Martínez Ávila, H., Hägg, D., & Gatenholm, P. (2015). 3D bioprinting human chondrocytes with nanocellulose-alginate bioink for cartilage tissue engineering applications. *Biomacromolecules, 16*(5), 1489–1496. https://doi.org/10.1021/acs.biomac.5b00188
Mirzaei, B. E., Ramazani, A., Shafiee, M., & Danaei, M. (2013). Studies on glutaraldehyde crosslinked chitosan hydrogel properties for drug delivery systems. *International Journal of Polymeric Materials and Polymeric Biomaterials, 62*(11), 605–611. https://doi.org/10.1080/00914037.2013.769165
Mohanty, C., & Sahoo, S. K. (2010). The in vitro stability and in vivo pharmacokinetics of curcumin prepared as an aqueous nanoparticulate formulation. *Biomaterials, 31*(25), 6597–6611. https://doi.org/10.1016/j.biomaterials.2010.04.062
Müller, M., Öztürk, E., Arlov, Ø., Gatenholm, P., & Zenobi-Wong, M. (2017). Alginate sulfate–nanocellulose bioinks for cartilage bioprinting applications. *Annals of Biomedical Engineering, 45*(1), 210–223. https://doi.org/10.1007/s10439-016-1704-5
Naseri, N., Poirier, J. M., Girandon, L., Fröhlich, M., Oksman, K., & Mathew, A. P. (2016). 3-Dimensional porous nanocomposite scaffolds based on cellulose nanofibers for cartilage tissue engineering: Tailoring of porosity and mechanical performance. *RSC Advances, 6*(8), 5999–6007. https://doi.org/10.1039/c5ra27246g
Ordikhani, F., Arslan, M. E., Marcelo, R., Sahin, I., Grigsby, P., Schwarz, J. K., & Azab, A. K. (2016). Drug delivery approaches for the treatment of cervical cancer. *Pharmaceutics, 8*(3), 1–15. https://doi.org/10.3390/pharmaceutics8030023
Pei, A., Malho, J. M., Ruokolainen, J., Zhou, Q., & Berglund, L. A. (2011). Strong nanocomposite reinforcement effects in polyurethane elastomer with low volume fraction of cellulose nanocrystals. *Macromolecules, 44*(11), 4422–4427. https://doi.org/10.1021/ma200318k
Placone, J. K., & Engler, A. J. (2018). Recent advances in extrusion-based 3D printing for biomedical applications. *Advanced Healthcare Materials, 7*(8), 1–11. https://doi.org/10.1002/adhm.201701161
Sanoj Rejinold, N., Muthunarayanan, M., Divyarani, V. V., Sreerekha, P. R., Chennazhi, K. P., Nair, S. V., Tamura, H., & Jayakumar, R. (2011). Curcumin-loaded biocompatible thermoresponsive polymeric nanoparticles for cancer drug delivery. *Journal of Colloid and Interface Science, 360*(1), 39–51. https://doi.org/10.1016/j.jcis.2011.04.006
Sarmento, B., Ferreira, D., Veiga, F., & Ribeiro, A. (2006). Characterization of insulin-loaded alginate nanoparticles produced by ionotropic pre-gelation through DSC and FTIR studies. *Carbohydrate Polymers, 66*(1), 1–7. https://doi.org/10.1016/j.carbpol.2006.02.008
Schwab, A., Levato, R., D'este, M., Piluso, S., Eglin, D., & Malda, J. (2020). Printability and shape fidelity of bioinks in 3D bioprinting. *Chemical Reviews, 120*(19), 11028–11055. https://doi.org/10.1021/acs.chemrev.0c00084
Segal, L., Creely, J. J., Martin, A. E., & Conrad, C. M. (1959). An empirical method for estimating the degree of crystallinity of native cellulose using the X-ray diffractometer. *Textile Research Journal, 29*(10), 786–794. https://doi.org/10.1177/004051755902901003
Siqueira, G., Kokkinis, D., Libanori, R., Hausmann, M. K., Gladman, A. S., Neels, A., Tingaut, P., Zimmermann, T., Lewis, J. A., & Studart, A. R. (2017). Cellulose nanocrystal inks for 3D printing of textured cellular architectures. *Advanced Functional Materials, 27*(12), Article 1604619. https://doi.org/10.1002/adfm.201604619
Sultan, S., Abdelhamid, H. N., Zou, X., & Mathew, A. P. (2019). CelloMOF: Nanocellulose enabled 3D printing of metal–rganic frameworks. *Advanced Functional Materials, 29* (2), 1–12. https://doi.org/10.1002/adfm.201805372
Tappa, K., & Jammalamadaka, U. (2018). Novel biomaterials used in medical 3D printing techniques. *Journal of Functional Biomaterials, 9*(1), 17. https://doi.org/10.3390/jfb9010017
Thiripura Sundari, M., & Ramesh, A. (2012). Isolation and characterization of cellulose nanofibers from the aquatic weed water hyacinth - Eichhornia crassipes. *Carbohydrate Polymers, 87*(2), 1701–1705. https://doi.org/10.1016/j.carbpol.2011.09.076
Wilson, S. A., Cross, L. M., Peak, C. W., & Gaharwar, A. K. (2017). Shear-thinning and thermo-reversible nanoengineered inks for 3D bioprinting. *ACS Applied Materials and Interfaces, 9*(50), 43449–43458. https://doi.org/10.1021/acsami.7b13602
Wu, X., Liu, Y., Li, X., Wen, P., Zhang, Y., Long, Y., Wang, X., Guo, Y., Xing, F., & Gao, J. (2010). Preparation of aligned porous gelatin scaffolds by unidirectional freeze-drying method. *Acta Biomaterialia, 6*(3), 1167–1177. https://doi.org/10.1016/j.actbio.2009.08.041
Yakub, G., Toncheva, A., Manolova, N., Rashkov, I., Danchev, D., & Kussovski, V. (2016). Electrospun polylactide-based materials for curcumin release: Photostability, antimicrobial activity, and anticoagulant effect. *Journal of Applied Polymer Science, 133*(5), 1–11. https://doi.org/10.1002/app.42940
Yallapu, M. M., Jaggi, M., & Chauhan, S. C. (2012). Curcumin nanoformulations: A future nanomedicine for cancer. *Drug Discovery Today, 17*(1–2), 71–80. https://doi.org/10.1016/j.drudis.2011.09.009
Yallapu, M. M., Jaggi, M., & Chauhan, S. C. (2010). β-Cyclodextrin-curcumin self-assembly enhances curcumin delivery in prostate cancer cells. *Colloids and Surfaces B: Biointerfaces, 79*(1), 113–125. https://doi.org/10.1016/j.colsurfb.2010.03.039